

# An improved scheme for calculating the bulk and surface Green's functions within quantum transport theory for systems with long unit cells: Application to carbon nanotubes

Fabian Teichert<sup>1,3,4</sup>, Andreas Zienert<sup>2</sup>, Jörg Schuster<sup>3,4</sup>, Michael Schreiber<sup>1,4</sup>

<sup>1</sup> Institute of Physics, Chemnitz University of Technology, 09107 Chemnitz, Germany

<sup>2</sup> Center for Microtechnologies, Chemnitz University of Technology, 09107 Chemnitz, Germany

<sup>3</sup> Fraunhofer Institute for Electronic Nano Systems (ENAS), 09126 Chemnitz, Germany

<sup>4</sup> Dresden Center for Computational Materials Science (DCMS), TU Dresden, 01062 Dresden, Germany

E-mail address: fabian.teichert@physik.tu-chemnitz.de

**Abstract:** We derive an improved version of the renormalization decimation algorithm (RDA) of López Sancho, which is used in quantum transport theory to calculate the bulk and the surface Green's function of a device. We consider the case of very long unit cells (in transport direction). This covers not only long unit cells itself but also supercell-like calculations for defective structures. For such large systems, short-range interactions lead to a sparse real space Hamiltonian matrix. We show how this and a corresponding subdivision of the unit cell in combination with the decimation technique can be used to previously reduce the system size. The result are separate RDA calculation of much smaller effective Hamiltonian matrices for each Green's function. Finally, we present the performance properties of our improved algorithm as well as some exemplary results for chiral carbon nanotubes.

Keywords: renormalization decimation algorithm (RDA); electronic transport; carbon nanotube (CNT)

## 1 Introduction

Simulation techniques have become an important role in determining material properties in the last decades. Mostly driven by the rapid progress in microelectronics, the resulting miniaturisation, and the search for better and new devices, the possibilities and the requirements of quantum simulation enhanced a lot. They are widely used for the theoretical investigation of possible effects in already synthesized materials. But also the discovery of complete new materials is possible. The today's computer power allows on a quantum-mechanical scale to scan through e.g. different ternary alloys of different element combinations all over the periodic system. Also the treatment of huge system in the mesoscopic range is possible, making investigations of long-range effects achievable. A third view is the inclusion of multiple effects like electron-electron interaction, electron-phonon interaction, spin-orbit coupling etc.

In the present study, we treat the topic of quantum transport simulations [1, 2], which is based on the computation of Green's functions. They are widely used for calculating e.g. the conductance of new metallic conductors, which could replace copper conductors, the performance of new field effect transistors (FET), which could replace common silicon-based FETs, and the functionality of sensors to include in situ measurements into devices. This work focuses on the treatment of huge system in the mesoscopic range and tries to reduce its computation time. As an underlying electron structure theory, density functional theory (DFT) [3, 4] can handle up to some thousands of atoms, but can still not reach the region of hundred thousand atoms. For this purpose, tight-binding (TB) models are often used. Whereas simple distant-independent nearest-neighbor models often only allow to get qualitatively correct results, the density-functional-based tight binding (DFTB) [5, 6] combines the fastness of TB calculations with DFT-like accuracy and thus allows to get quantitative correct results. Many DFTB parameter sets have been developed to describe different systems correctly, organic molecules on the one side, metals on the other side, but also their interplay in mixed systems like devices which connect organic molecules to metallic electrodes. Such DFTB models then allow to calculate the electronic structure and the electronic transport of mesoscopic systems. Examples are random disordered systems [7–13]. They are often treated with recursive or iterative techniques. The linear scaling recursive Green's function formalism (RGF) [14–17] and the logarithmic scaling renormalization decimation algorithm of López Sancho et al. [18, 19] can be used to calculate the transmission through a device. Both algorithms use a decimation idea of subdividing the total system into slices. Long unit cells can be further subdivided and it is clear how to proceed for the RGF. But as the RDA requires periodicity, it has to be rewritten to also get an improvement here. In the following work we consider this problem and show how the RDA can be adapted to systems with long unit cells to gain calculation speed.

First, we derive the equations of the improved RDA to calculate the electrode's left/right surface Green's functions, the bulk Green's function, the transmission and the bulk density of states. Second, we show the scaling of the complexity. For this, we perform computations for chiral carbon nanotubes with different unit cell lengths to verify the complexity dependencies for one example. Finally, we depict some exemplary results for (10,1) and (10,9) carbon nanotubes.

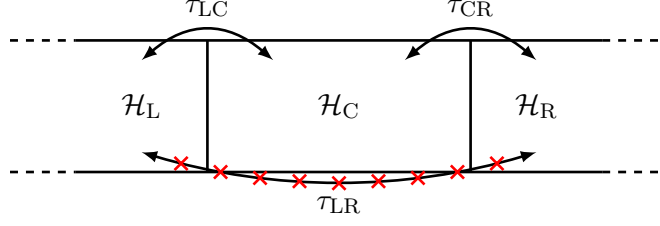


**Fig. 1:** (Color online.) Device scheme [10]. A infinite long system is divided into a finite central region C and two half-infinite electrodes L (left) and R (right), to which C is connected. L and R are periodic. C contains an arbitrary scattering region.  $\mathcal{H}_{L/C/R}$  are the Hamiltonian matrices of the corresponding part L/C/R.  $\tau_{LC/CR/LR}$  are the coupling matrices connecting two of these parts.

## 2 Electronic transport

In this section we give a brief overview about the common equilibrium quantum transport theory [1], which tells us how to calculate electronic properties like density of states, electron density, transmission, and conductance. Let us consider a device system, shown in fig. 1. This is an infinite system with a scattering region at the center (C), which is finite in transport direction, and periodic half-infinite regions to the left (L) and the right (R) of C, the electrodes. These electrodes act as the reservoirs of an open system and provide electrons, which are transmitted through the system and scattered within the scattering region C. For such a device, the Schrödinger equation within a real space non-orthogonal basis reads

$$\mathcal{H}_{\text{tot}} \Psi = \begin{pmatrix} \mathcal{H}_L & \tau_{LC} & \\ \tau_{CL} & \mathcal{H}_C & \tau_{CR} \\ & \tau_{RC} & \mathcal{H}_R \end{pmatrix} \Psi = E \mathcal{S}_{\text{tot}} \Psi = E \begin{pmatrix} \mathcal{S}_L & \mathcal{S}_{LC} & \\ \mathcal{S}_{CL} & \mathcal{S}_C & \mathcal{S}_{CR} \\ & \mathcal{S}_{RC} & \mathcal{S}_R \end{pmatrix} \Psi \quad . \quad (1)$$

$\mathcal{H}_{L/C/R}$  is the Hamiltonian matrix of the corresponding region (left electrode, central region, right electrode).  $\tau_{LC/CL/RC/CR}$  are the Hamiltonian coupling matrices between two of these regions. If the central region is large enough, i.e. larger than the maximum interaction distance, the coupling between L and R can be neglected,  $\tau_{LR/RL} = 0$ .  $\mathcal{S}_{L/C/R}$  are the corresponding overlap matrices for the regions L, C, and R.  $\mathcal{S}_{LC/CL/RC/CR}$  are the overlap matrices for the coupling of two of these regions. For fixed  $E$ , we can get rid of the  $\mathcal{S}$ -terms by hiding them in the  $\mathcal{H}$ - and  $\tau$ -terms with the substitution

$$\mathcal{H} := \mathcal{H} - E(\mathcal{S} - \mathcal{I}) \quad , \quad \tau := \tau - E\mathcal{S} \quad . \quad (2)$$

$\mathcal{I}$  is the identity matrix of appropriate dimension. After this, 1 transforms in an orthonormal-like equation with the new  $\mathcal{H}$  and  $\tau$ , which will be used within all subsequent explanations.

Equation (1) has infinite matrix dimensions, but can be reduced to a problem of finite dimension by calculation the perturbed Green's function of the central region

$$\mathcal{G}_C = [(E + i\eta)\mathcal{I} - \mathcal{H}_C - \Sigma_L - \Sigma_R]^{-1} \quad . \quad (3)$$

Here, the difficulty of treating infinite systems is shifted to the calculation of the self-energies  $\Sigma_L = \tau_{CL}\mathcal{G}_L\tau_{LC}$  and  $\Sigma_R = \tau_{CR}\mathcal{G}_R\tau_{RC}$ , which leads to energetic shifts of the electronic states within C due to the coupling to the left and right electrode. The surface Green's function of the left electrode  $\mathcal{G}_R$  and the right electrode  $\mathcal{G}_L$  can be calculated iteratively with the RDA shown in sec. 3 (note that indices switched here because for simplicity in the further sections,  $\mathcal{G}_L$  denotes the left end of the electrode and thus corresponds to the surface of the right electrode and vice versa).

With the use of the Green's function the transmission spectrum can be calculated via

$$\mathcal{T}(E) = \text{Tr} \left( \Gamma_R \mathcal{G}_C \Gamma_L \mathcal{G}_C^\dagger \right) \quad . \quad (4)$$

The broadening matrices  $\Gamma_{L/R} = i(\Sigma_{L/R} - \Sigma_{L/R}^\dagger)$  lead to a broadening of the electronic states within C due to the coupling to the electrodes. The conductance of the total system can be calculated using the Landauer-Büttiker formalism [2]

$$G = -G_0 \int_{-\infty}^{\infty} \mathcal{T}(E) f'(E) dE \quad \text{with} \quad G_0 = \frac{2e^2}{h} \quad \text{and} \quad f(E) = \frac{1}{1 + \exp\left(\frac{E - E_F}{k_B T}\right)} \quad . \quad (5)$$

$E_F$  is the Fermi energy.

### 3 Decimation technique and renormalization decimation algorithm

The RDA was derived by López Sancho et al. [18, 19]. It is an iterative algorithm to calculate the bulk and surface Green's functions ( $\mathcal{G}_{B/L/R}$ ) of periodic systems, e.g. the electrodes of a device described above. The real space Hamiltonian matrix of the electrode is periodic, because the electrode is periodic. Assuming short range interaction it is also block-wise tridiagonal. Considering a large, but finite system, the electrode Hamiltonian matrix and the corresponding Green's matrix read

$$\mathcal{H}_{\text{el}} = \begin{pmatrix} \mathcal{H} & \tau & & & \\ \tau^\dagger & \mathcal{H} & \tau & & \\ & \tau^\dagger & \ddots & \ddots & \\ & & \ddots & \mathcal{H} & \tau \\ & & & \tau^\dagger & \mathcal{H} \end{pmatrix} \quad \text{and} \quad \mathcal{G}_{\text{el}} = \begin{pmatrix} \mathcal{G}_L & \cdots & \cdots & & \\ \vdots & \ddots & \ddots & & \\ \vdots & \ddots & \mathcal{G}_B & \ddots & \vdots \\ & & \ddots & \ddots & \\ & & \cdots & \cdots & \mathcal{G}_R \end{pmatrix}. \quad (6)$$

$\mathcal{H}$  is the Hamiltonian matrix of one periodic unit cell.  $\tau$  is the Hamiltonian coupling matrix between adjacent unit cells.  $\mathcal{G}_B$  is the bulk Green's matrix corresponding to the bulk-like periodic region far away from the finite ends.  $\mathcal{G}_L$  is the surface Green's matrix of the left surface and  $\mathcal{G}_R$  the one of the right surface. As only the three mentioned Green's matrix blocks are of interest, the decimation technique can be used to reduce the inversion problem of the total system to an inversion problem of a smaller effective system containing the relevant parts and ignoring the rest.

At first, let us consider a given  $(3 \times 3)$ -matrix  $A$  and its unknown inverse  $B$ . Let us further assume that the upper left and lower right entry  $B_{11}$  and  $B_{33}$  of  $B$  have to be calculated. For that, the  $(3 \times 3)$ -inversion-problem

$$\begin{pmatrix} A_{11} & A_{12} & A_{13} \\ A_{21} & A_{22} & A_{23} \\ A_{31} & A_{32} & A_{33} \end{pmatrix} \begin{pmatrix} B_{11} & B_{12} & B_{13} \\ B_{21} & B_{22} & B_{23} \\ B_{31} & B_{32} & B_{33} \end{pmatrix} = \begin{pmatrix} 1 & 0 & 0 \\ 0 & 1 & 0 \\ 0 & 0 & 1 \end{pmatrix} \quad (7)$$

can be reduced to the  $(2 \times 2)$ -inversion-problem

$$A_{\text{eff}} \begin{pmatrix} B_{11} & B_{13} \\ B_{31} & B_{33} \end{pmatrix} = \begin{pmatrix} 1 & 0 \\ 0 & 1 \end{pmatrix}. \quad (8)$$

Comparing both, the effective matrix  $A_{\text{eff}}$  yields

$$A_{\text{eff}} = \begin{pmatrix} A_{11} & A_{13} \\ A_{31} & A_{33} \end{pmatrix} + \begin{pmatrix} A_{12} \\ A_{32} \end{pmatrix} A_{22}^{-1} \begin{pmatrix} A_{21} & A_{23} \end{pmatrix} = \begin{pmatrix} A_{11} + A_{12} A_{22}^{-1} A_{21} & A_{13} + A_{12} A_{22}^{-1} A_{23} \\ A_{31} + A_{32} A_{22}^{-1} A_{21} & A_{33} + A_{32} A_{22}^{-1} A_{23} \end{pmatrix}. \quad (9)$$

Applying the latter to the electrode Hamiltonian and Green's matrix, an iterative algorithm can be derived, where  $A_{13} = A_{31} = 0$  because of the absence of coupling beyond adjacent cells. By divide and conquer the RDA can be achieved. An electrode with  $2^k + 1$  unit cells is considered and each second cell is decimated in each step until only three cells are left. They correspond to the left/bulk/right Green's matrix. This leads to the following equations:

$$\mathcal{G}_B^{(i)} = \left[ (E + i\eta)\mathcal{I} - \mathcal{H}_B^{(i)} \right]^{-1} \quad \text{with} \quad \mathcal{H}_{L/B/R}^{(0)} = \mathcal{H}, \quad (10a)$$

$$\alpha^{(i+1)} = \alpha^{(i)} \mathcal{G}_B^{(i)} \alpha^{(i)} \quad \text{with} \quad \alpha^{(0)} = \tau, \quad (10b)$$

$$\beta^{(i+1)} = \beta^{(i)} \mathcal{G}_B^{(i)} \beta^{(i)} \quad \text{with} \quad \beta^{(0)} = \tau^\dagger, \quad (10c)$$

$$\mathcal{H}_L^{(i+1)} = \mathcal{H}_L^{(i)} + \alpha^{(i)} \mathcal{G}_B^{(i)} \beta^{(i)}, \quad (10d)$$

$$\mathcal{H}_B^{(i+1)} = \mathcal{H}_B^{(i)} + \alpha^{(i)} \mathcal{G}_B^{(i)} \beta^{(i)} + \beta^{(i)} \mathcal{G}_B^{(i)} \alpha^{(i)}, \quad (10e)$$

$$\mathcal{H}_R^{(i+1)} = \mathcal{H}_R^{(i)} + \beta^{(i)} \mathcal{G}_B^{(i)} \alpha^{(i)}. \quad (10f)$$

The effective Hamiltonian matrices  $\mathcal{H}_{L/R}^{(i)}$  correspond to the first/last diagonal elements of (9) and get a correction because they are connected to a right/left cell. The effective bulk Hamiltonian matrix  $\mathcal{H}_B^{(i)}$  gets both corrections because it is connected to both, a left and a right cell. The effective coupling matrices  $\alpha^{(i)}$  and  $\beta^{(i)}$  correspond to the upper and lower non-diagonal element of (9). The whole RDA is an iterative algorithm and  $\mathcal{H}_{L/B/R}^{(i)}$  can be assumed as converged if  $\|\alpha\| + \|\beta\| \rightarrow 0$ . Finally, the bulk/surface Green's matrix can be calculated with

$$\mathcal{G}_{L/B/R} = \left[ (E + i\eta)\mathcal{I} - \mathcal{H}_{L/B/R}^{(\infty)} \right]^{-1}. \quad (11)$$

A sketch of the RDA is shown in fig. 2.

For the  $2^k + 1$  cells,  $k - 1$  inversions and  $6k - 6$  multiplications have to be done. Considering  $N$  cells,  $\log_2(N - 1) - 1$  inversions and  $6\log_2(N - 1) - 6$  multiplications have to be done. This logarithmic scaling complexity leads to very fast convergence.

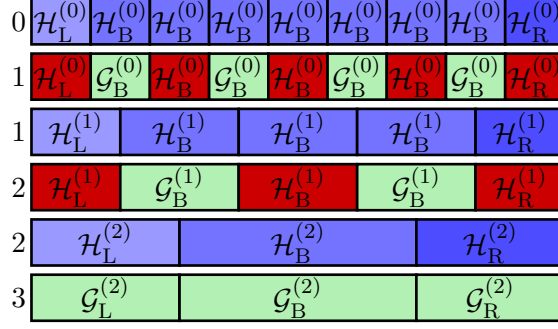


**Fig. 2:** (Color online.) Sketch of the RDA for an example-electrode with 9 unit cells. The numbers to the left of each row denote the iteration step  $i$  within (10). Blue blocks denote the Hamiltonian matrices. The different brightness denotes the differences between L, B, and R. Green blocks denote the Green's matrices of the cells which are decimated within the actual iteration step. Red blocks denote Hamiltonian matrices which get a correction due to the coupling the decimated adjacent cells.

#### 4 Renormalization decimation algorithm for electrodes with long unit cells

The RDA includes the calculation of the Green's function of the unit cell, which is a inversion. Its complexity scales as  $\mathcal{O}((\dim \mathcal{H})^3)$ , getting worse for large unit cells. But in cases where the unit cell is long in transport direction, the short range interaction leads also to a block-wise tridiagonal unit cell Hamiltonian matrix the same way as the block-wise tridiagonal electrode Hamiltonian matrix itself, but not periodic. Thus, the unit cell can be divided into  $K$  slices. The total electrode Hamiltonian and Green's matrix are still described by (6). Furthermore, the unit cell Hamiltonian matrix, the coupling matrix, and the total bulk Green's matrix have the following  $(K \times K)$ -shape:

$$\mathcal{H} = \begin{pmatrix} \mathcal{H}_1 & \tau_{12} & & \\ \tau_{21} & \mathcal{H}_2 & \tau_{23} & \\ & \tau_{32} & \ddots & \ddots \\ & & \ddots & \mathcal{H}_K \end{pmatrix}, \quad \tau = \begin{pmatrix} & & & \\ & & & \\ & & & \\ \tau_{K1} & & & \end{pmatrix}. \quad (12)$$

##### 4.1 Surface Green's functions

The surface Green's functions  $\mathcal{G}_{L/R}$  of (6), which are necessary for transport calculations, are now much smaller ones, corresponding to the surface blocks  $\mathcal{H}_1$  (for L) and  $\mathcal{H}_K$  (for R). Using the decimation technique one can get rid of  $\mathcal{H}_i$  for  $i = 2, \dots, K-1$ :

$$\mathcal{G}_i = \left[ (E - i\eta)\mathcal{I} - \tilde{\mathcal{H}}_i \right]^{-1} \quad \text{with} \quad \tilde{\mathcal{H}}_2 = \mathcal{H}_2 \quad (13a)$$

$$\tilde{\mathcal{H}}_1^{(i)} = \tilde{\mathcal{H}}_1^{(i-1)} + \tilde{\tau}_{1i} \mathcal{G}_i \tilde{\tau}_{i1} \quad \text{with} \quad \tilde{\mathcal{H}}_1^{(0)} = \mathcal{H}_1, \quad (13b)$$

$$\tilde{\mathcal{H}}_{i+1} = \mathcal{H}_{i+1} + \tau_{(i+1)i} \mathcal{G}_i \tau_{i(i+1)}, \quad (13c)$$

$$\tilde{\tau}_{1(i+1)} = \tilde{\tau}_{1i} \mathcal{G}_i \tau_{i(i+1)} \quad \text{with} \quad \tilde{\tau}_{12} = \tau_{12}, \quad (13d)$$

$$\tilde{\tau}_{(i+1)1} = \tau_{(i+1)i} \mathcal{G}_i \tilde{\tau}_{i1} \quad \text{with} \quad \tilde{\tau}_{21} = \tau_{21}. \quad (13e)$$

This results in an effective periodic two-part system

$$\mathcal{H}_{\text{el}}^{\text{eff}} = \begin{pmatrix} \mathcal{L} & \sigma_{\mathcal{L}\mathcal{R}} & & & \\ \sigma_{\mathcal{R}\mathcal{L}} & \mathcal{R} & \tau_{\mathcal{R}\mathcal{L}} & & \\ & \tau_{\mathcal{L}\mathcal{R}} & \mathcal{L} & \sigma_{\mathcal{L}\mathcal{R}} & \\ & & \sigma_{\mathcal{R}\mathcal{L}} & \mathcal{R} & \tau_{\mathcal{R}\mathcal{L}} \\ & & \tau_{\mathcal{L}\mathcal{R}} & \ddots & \ddots \\ & & & \ddots & \mathcal{L} & \sigma_{\mathcal{L}\mathcal{R}} \\ & & & & \sigma_{\mathcal{R}\mathcal{L}} & \mathcal{R} \end{pmatrix} \quad (14)$$

with effective left matrices  $\mathcal{L} = \tilde{\mathcal{H}}_1^{(K-1)}$ , effective right matrices  $\mathcal{R} = \tilde{\mathcal{H}}_K$ , and effective coupling matrices  $\sigma_{\mathcal{L}\mathcal{R}} = \tilde{\tau}_{1K}$ ,  $\sigma_{\mathcal{R}\mathcal{L}} = \tilde{\tau}_{K1}$ ,  $\tau_{\mathcal{R}\mathcal{L}} = \tau_{K1}$ , and  $\tau_{\mathcal{L}\mathcal{R}} = \tau_{1K}$ .

The surface Green's matrices of the effective two-part system can be evaluated by doing two separate RDA calculations. First, the left surface  $\mathcal{G}_L$  can be calculated the following way: The decimation of all  $\mathcal{R}$  leads to a new effective

periodic Hamiltonian matrix, except the lower right block (in which we are not interested at this time). Consequently, the RDA (10) can be applied to this by using the resulting initial values

$$\mathcal{G}_{\mathcal{R}} = [(E + i\eta)\mathcal{I} - \mathcal{R}]^{-1} , \quad (15a)$$

$$\mathcal{H}_{\mathcal{L}}^{(0)} = \mathcal{L} + \sigma_{\mathcal{L}\mathcal{R}}\mathcal{G}_{\mathcal{R}}\sigma_{\mathcal{R}\mathcal{L}} , \quad (15b)$$

$$\mathcal{H}_{\mathcal{B}}^{(0)} = \mathcal{L} + \sigma_{\mathcal{L}\mathcal{R}}\mathcal{G}_{\mathcal{R}}\sigma_{\mathcal{R}\mathcal{L}} + \tau_{\mathcal{L}\mathcal{R}}\mathcal{G}_{\mathcal{R}}\tau_{\mathcal{R}\mathcal{L}} , \quad (15c)$$

$$\alpha^{(0)} = \sigma_{\mathcal{L}\mathcal{R}}\mathcal{G}_{\mathcal{R}}\tau_{\mathcal{R}\mathcal{L}} , \quad (15d)$$

$$\beta^{(0)} = \tau_{\mathcal{L}\mathcal{R}}\mathcal{G}_{\mathcal{R}}\sigma_{\mathcal{R}\mathcal{L}} . \quad (15e)$$

The execution of (10f) is not necessary. Afterwards,  $\mathcal{G}_{\mathcal{L}}$  is determined by (11). Second, the right surface  $\mathcal{G}_{\mathcal{R}}$  can be calculated the following way: The decimation of all  $\mathcal{L}$  leads to a new effective periodic Hamiltonian matrix, except the upper left block (in which we are also not interested at this time). Consequently, the RDA (10) can be applied a second time to this by using the resulting initial values

$$\mathcal{G}_{\mathcal{L}} = [(E + i\eta)\mathcal{I} - \mathcal{L}]^{-1} , \quad (16a)$$

$$\mathcal{H}_{\mathcal{R}}^{(0)} = \mathcal{R} + \sigma_{\mathcal{R}\mathcal{L}}\mathcal{G}_{\mathcal{L}}\sigma_{\mathcal{L}\mathcal{R}} , \quad (16b)$$

$$\mathcal{H}_{\mathcal{B}}^{(0)} = \mathcal{R} + \sigma_{\mathcal{R}\mathcal{L}}\mathcal{G}_{\mathcal{L}}\sigma_{\mathcal{L}\mathcal{R}} + \tau_{\mathcal{R}\mathcal{L}}\mathcal{G}_{\mathcal{L}}\tau_{\mathcal{L}\mathcal{R}} , \quad (16c)$$

$$\alpha^{(0)} = \tau_{\mathcal{R}\mathcal{L}}\mathcal{G}_{\mathcal{L}}\sigma_{\mathcal{L}\mathcal{R}} , \quad (16d)$$

$$\beta^{(0)} = \sigma_{\mathcal{R}\mathcal{L}}\mathcal{G}_{\mathcal{L}}\tau_{\mathcal{L}\mathcal{R}} . \quad (16e)$$

As well here, the execution of (10d) is not necessary. Afterwards,  $\mathcal{G}_{\mathcal{R}}$  is determined by (11). Because the RDA has to be done twice, we call the total algorithm Dual-RDA. A sketch of this is shown in fig. 3.

## 4.2 Bulk Green's functions and electrode density of states

For the long unit cell consisting of  $K$  slices, the total periodic Green's function reads

$$\mathcal{G}_{\text{el}} = \begin{pmatrix} \ddots & \ddots & \ddots & \ddots & \ddots & \ddots & \ddots & \ddots & \ddots & \ddots \\ \ddots & \mathcal{G}_{11} & \mathcal{G}_{12} & \ddots & \ddots & \ddots & \ddots & \ddots & \ddots & \ddots \\ \ddots & \mathcal{G}_{21} & \mathcal{G}_{22} & \ddots & \ddots & \ddots & \ddots & \ddots & \ddots & \ddots \\ \ddots & \ddots & \ddots & \ddots & \mathcal{G}_{(K-1)K} & \ddots & \ddots & \ddots & \ddots & \ddots \\ \ddots & \ddots & \ddots & \mathcal{G}_{K(K-1)} & \mathcal{G}_{KK} & \mathcal{G}_{K1} & \ddots & \ddots & \ddots & \ddots \\ \ddots & \ddots & \ddots & \ddots & \mathcal{G}_{1K} & \mathcal{G}_{11} & \mathcal{G}_{12} & \ddots & \ddots & \ddots \\ \ddots & \ddots & \ddots & \ddots & \ddots & \mathcal{G}_{21} & \mathcal{G}_{22} & \ddots & \ddots & \ddots \\ \ddots & \ddots & \ddots & \ddots & \ddots & \ddots & \ddots & \ddots & \mathcal{G}_{(K-1)K} & \ddots \\ \ddots & \ddots & \ddots & \ddots & \ddots & \ddots & \ddots & \mathcal{G}_{K(K-1)} & \mathcal{G}_{KK} & \ddots \\ \ddots & \ddots & \ddots & \ddots & \ddots & \ddots & \ddots & \ddots & \ddots & \ddots \end{pmatrix} . \quad (17)$$

The density of states (DOS) of each electrode as a representative for the electronic structure can be calculated with

$$\mathcal{D}_{\text{el}}(E) = -\frac{1}{\pi} \text{Im} \text{Tr} (\mathcal{G}_{\text{el}} \mathcal{S}_{\text{el}})_{\text{B}} = -\frac{1}{\pi} \sum_{i=1}^K \text{Im} [\text{Tr} (\mathcal{G}_{ii} \mathcal{S}_{ii}) + \text{Tr} (\mathcal{G}_{ij} \mathcal{S}_{ji}) + \text{Tr} (\mathcal{G}_{ji} \mathcal{S}_{ij})] , \quad (18)$$

where  $j = (i + 1) \bmod K$ . Considering cell  $i$  as the most right slice and slice  $j$  as the most left slice, the slices  $j + 1 \dots i - 1$  have to be decimated, similar to (13). This leads to the following effective overall bulk Hamiltonian matrix and Green's function.

$$\begin{pmatrix} \ddots & \ddots & & & & & \\ \ddots & E - \mathcal{L}_j & -\sigma_{ji} & & & & \\ & -\sigma_{ij} & E - \mathcal{R}_i & -\tau_{ij} & & & \\ & & -\tau_{ji} & E - \mathcal{L}_j & -\sigma_{ji} & & \\ & & & -\sigma_{ij} & E - \mathcal{R}_i & \ddots & \\ & & & & \ddots & \ddots & \end{pmatrix} \begin{pmatrix} \ddots & \ddots & \ddots & \ddots & \ddots & \ddots \\ \ddots & \mathcal{G}_{jj} & \ddots & \ddots & \ddots & \ddots \\ \ddots & \ddots & \mathcal{G}_{ii} & \mathcal{G}_{ij} & \ddots & \ddots \\ \ddots & \ddots & \mathcal{G}_{ji} & \mathcal{G}_{jj} & \ddots & \ddots \\ \ddots & \ddots & \ddots & \ddots & \mathcal{G}_{ii} & \ddots \\ \ddots & \ddots & \ddots & \ddots & \ddots & \ddots \end{pmatrix} = \mathcal{I} \quad (19)$$

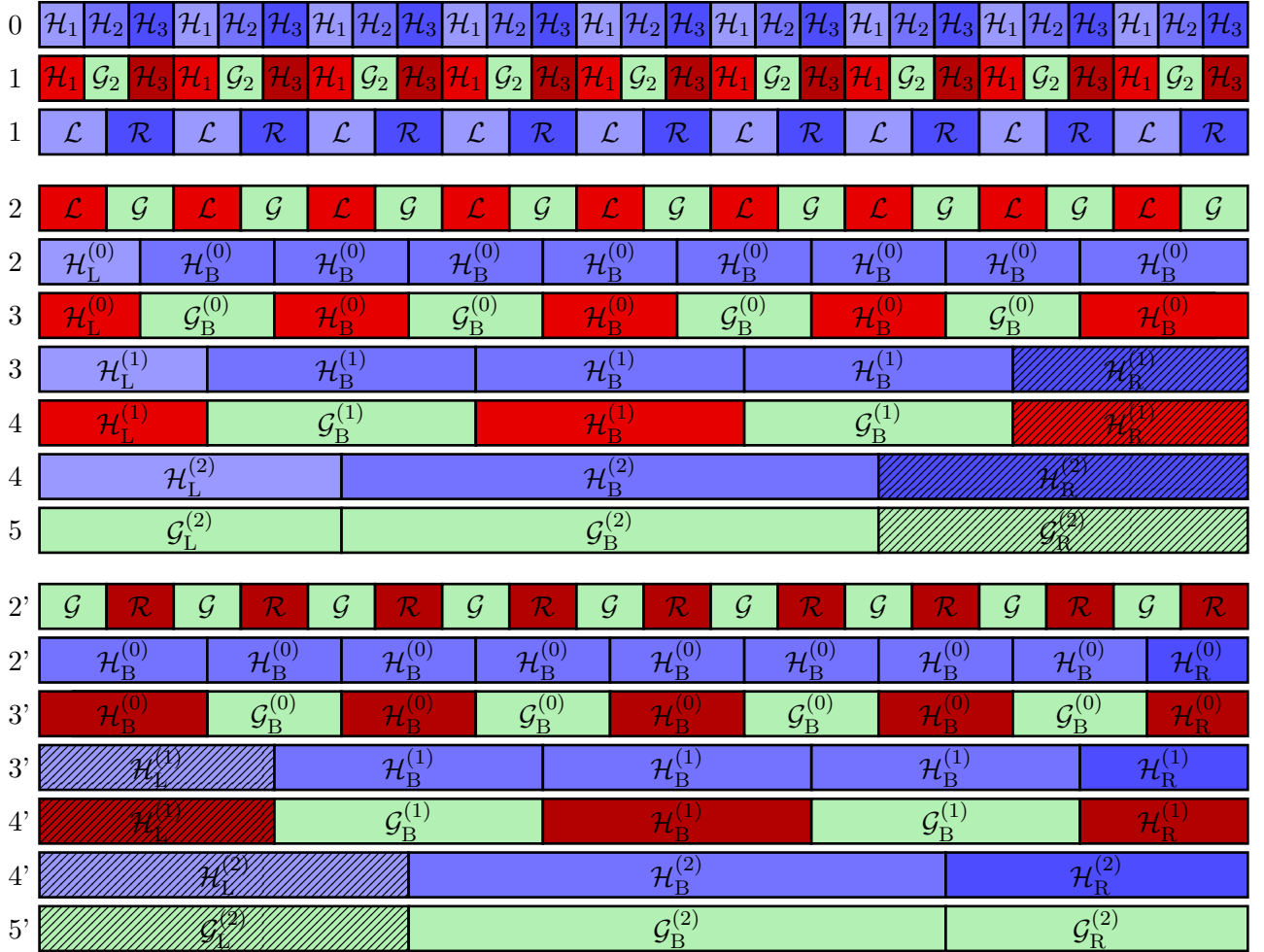


**Fig. 3:** (Color online.) Sketch of the Dual-RDA for an example-electrode with 9 unit cells, which are divided into 3 sub-cells. The upper rows correspond to the previous decimation steps getting an effective two-part system. The middle rows correspond to the RDA getting the Green's matrix of the left surface. The lower rows correspond to the RDA getting the Green's matrix of the right surface. The numbers to the left of each row denote the iteration step. Blue blocks denote the Hamiltonian matrices. The different brightness denotes the differences between L, B, and R. Green blocks denote the Green's matrices of the cells which are decimated within the actual iteration step. Red blocks denote Hamiltonian matrices which get a correction due to the coupling the decimated adjacent cells. The different brightness denotes the differences between L and R. Patterned blocks are unnecessary and will not be calculated.

Focusing on the center  $2 \times 2$  matrix block, decimating the  $\mathcal{L}_j$  in the left half-infinite part, decimating the  $\mathcal{R}_i$  in the right half-infinite part, and applying the RDA to both parts yields

$$\begin{pmatrix} \ddots & & & & & \\ & E - \mathcal{H}_{i,B}^{(\infty)} & & & & \\ \ddots & & 0 & & & \\ & 0 & E - \mathcal{H}_{i,R}^{(\infty)} & -\tau_{ij} & & \\ & & -\tau_{ji} & E - \mathcal{H}_{j,L}^{(\infty)} & & \\ & & & 0 & & \\ & & & 0 & E - \mathcal{H}_{j,B}^{(\infty)} & \ddots \\ & & & & & \ddots \end{pmatrix} \begin{pmatrix} \ddots & \ddots & \ddots & \ddots \\ \ddots & \mathcal{G}_{ii} & \mathcal{G}_{ij} & \ddots \\ \ddots & \mathcal{G}_{ji} & \mathcal{G}_{jj} & \ddots \\ \ddots & \ddots & \ddots & \ddots \end{pmatrix} = \mathcal{I} \quad . \quad (20)$$

Now, the center  $2 \times 2$  matrix block can be solved in an isolated way to get the necessary diagonal elements and first upper/lower non-diagonal elements

$$\mathcal{G}_{ii} = \left[ (E - i\eta)\mathcal{I} - \mathcal{H}_{i,\text{R}}^{(\infty)} - \tau_{ij}\mathcal{G}_{j,\text{L}}\tau_{ji} \right]^{-1} \quad , \quad (21\text{a})$$

$$\mathcal{G}_{jj} = \left[ (E - i\eta)\mathcal{I} - \mathcal{H}_{j,L}^{(\infty)} - \tau_{ji}\mathcal{G}_i\tau_{ij} \right]^{-1}, \quad (21b)$$

$$\mathcal{G}_{ij} = \mathcal{G}_{i,\text{R}} \tau_{ij} \mathcal{G}_{jj} \quad , \quad (21\text{c})$$

$$\mathcal{G}_{ji} = \mathcal{G}_{j,L} \tau_{ji} \mathcal{G}_{ii} \quad . \quad (21d)$$



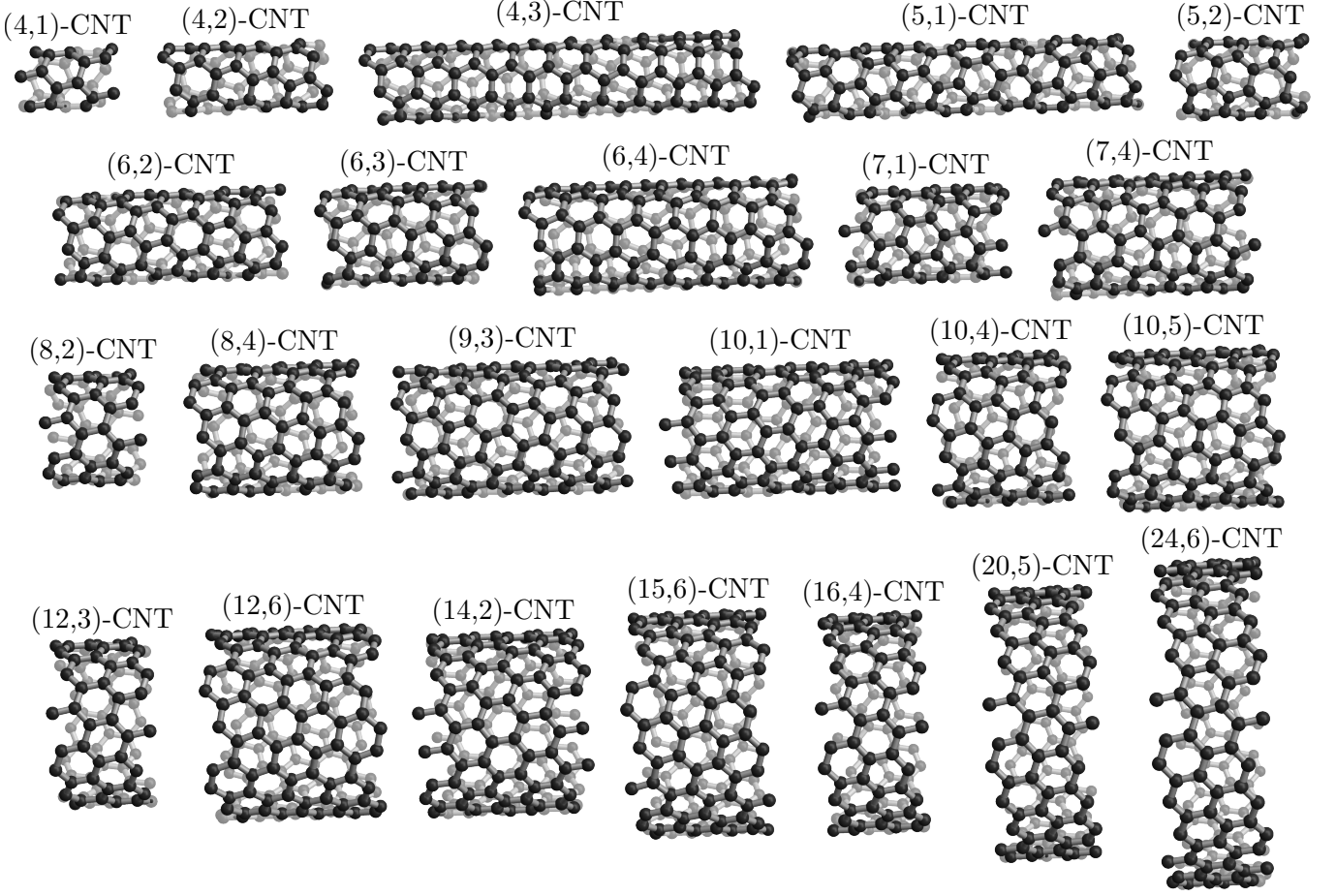


**Fig. 4:** CNT unit cells to which the RDA and the Dual-RDA is applied for the performance test.

In Summary, for each  $1 \leq i \leq K$  the decimations similar to (13), the RDA, and the final calculations (21) have to be done to get all the values to calculate the electrode DOS. Because the RDA has to be done  $K$  times, we call the total algorithm Multiple-RDA. To note, the quantities which are necessary for electron transport, namely the surface Green's functions, are included:

$$\mathcal{G}_L = \left[ (E - i\eta)\mathcal{I} - \mathcal{H}_{1,L}^{(\infty)} \right]^{-1}, \quad (22a)$$

$$\mathcal{G}_R = \left[ (E - i\eta)\mathcal{I} - \mathcal{H}_{K,R}^{(\infty)} \right]^{-1}. \quad (22b)$$

## 5 Complexity measure and performance test

In the following, the Dual-RDA resp. Multiple-RDA is compared to the conventional RDA by calculating the surface Green's functions resp. bulk Green's functions for 1000 energies. For this, we look at their complexity measures concerning the calculation time  $t$  and the memory requirement (RAM)  $m$  of a self-written C++ implementation using LAPACK routines [20]. We apply the algorithms to chiral carbon nanotubes, shown in fig. 4. Different diameters and different chiralities, which strongly affect the unit cell length, are addressed. Their number of subdivisions differs from  $K = 2$  to  $K = 9$ . Because the chiral carbon nanotubes are semiconducting, their bandgap depends on the diameter and the chirality. In energy regions within the bandgap with nearly no transmission, the RDA converges faster than in other energy regions. Therefore, we focus on 1000 energies outside the bandgap to get comparable calculation times for different CNTs.

The results for the Dual-RDA compared to the RDA are shown in fig. 5. (a) shows the calculation time and (b) the memory requirement. First of all, it can be seen that for all chiral CNTs the calculation time and the memory requirement is reduced drastically by at least a factor of 3 for the shortest CNT unit cells up to a factor of 176 for the longest CNT unit cells studied here. But it is not limited to that. Even longer unit cells can lead to even larger reductions. The exact dependence can be well described by the corresponding complexity measure, which is explained as follows. The complexity measure of the calculation time is characterized by the number of arithmetic operations. The RDA needs 1 matrix inversion, 6 matrix multiplications, and 4 matrix additions each iteration step

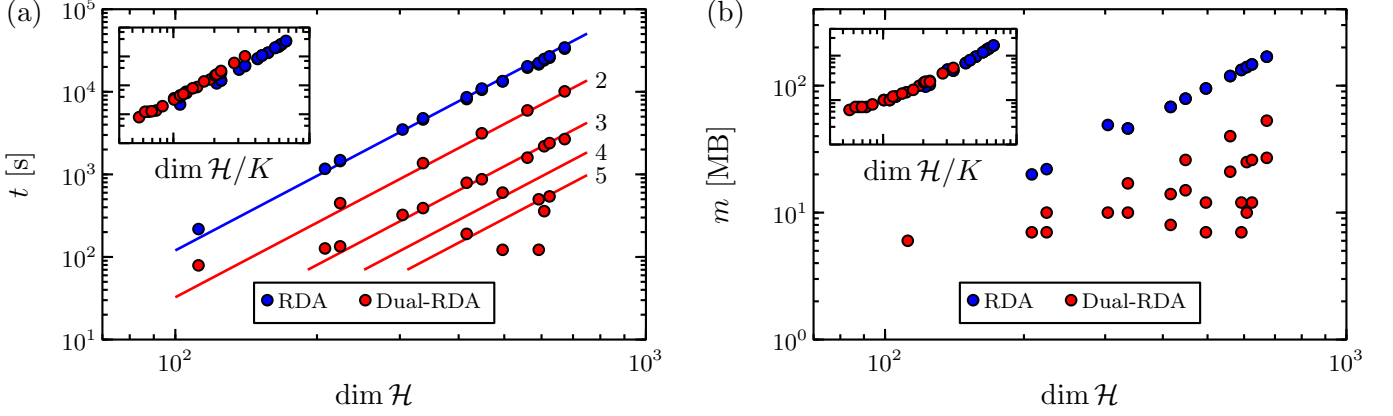


**Fig. 5:** (Color online.) (a) Calculation time and (b) memory requirement (RAM) for the conventional RDA (blue) and the Dual-RDA for long unit cells (red) when only calculating the surface Green's functions. The algorithms are applied to the different CNTs shown in fig. 4. The solid lines correspond to the complexity measures (23) and (25) with  $K$  written next to the corresponding line. The inset shows the same data, where the dimension of the unit cell Hamiltonian matrix is scaled with the number of sub-cells  $K$  ( $K = 1$  for the RDA,  $K = 2 \dots 7$  for the Dual-RDA).

and  $a$  iterations in total. For the CNTs we usually get convergence after approximately 15 to 25 iterations. The dominant operations are the matrix inversions, which scale approximately with the third power of the dimension. This leads to

$$t_{\text{RDA}} \sim a (\dim \mathcal{H})^3. \quad (23)$$

The complexity measure of the RAM is characterized by the number of allocated bytes. During the RDA, 5 matrices ( $\mathcal{H}_{\text{L/B/R}}$ ,  $\alpha$ , and  $\beta$ ), which are updated each iteration step, are stored. 3 additional RDA matrices are stored to omit repeating the same matrix multiplications. This leads to

$$m_{\text{RDA}} \sim 8 (\dim \mathcal{H})^2. \quad (24)$$

Both complexity measures are expressed in fig. 5 by the linear dependence in the log-log-scale (blue data points). An increase of 1 order of magnitude of  $\dim \mathcal{H}$  leads to an increase of 3 orders of magnitude in  $t$  and 2 orders of magnitude in  $m$ .

The complexity measures of the Dual-RDA described in sec. 4.2 can be similarly obtained. The Dual-RDA needs  $K$  decimation steps and 2 RDA executions. Each decimation step needs 1 matrix inversions, 6 matrix multiplications, 2 matrix additions. In total this yields  $K + 2a$  matrix inversions,  $6K + 12a$  matrix multiplications, and  $2K + 8a$  matrix additions. In comparison to the RDA, here the dimension of the matrices is much smaller. To get the most fast algorithm, the  $K$  slices should be as short as possible and thus the corresponding matrices have similar dimension. So, we can assume that the dimension of each matrix is a factor of  $K$  smaller than  $\dim \mathcal{H}$ . This leads to

$$t_{\text{Dual-RDA}} \sim (K + 2a) \left( \frac{\dim \mathcal{H}}{K} \right)^3 \stackrel{K \ll a}{\sim} 2a \left( \frac{\dim \mathcal{H}}{K} \right)^3, \quad (25a)$$

$$\stackrel{K \gg a}{\sim} K \left( \frac{\dim \mathcal{H}}{K} \right)^3. \quad (25b)$$

During the Dual-RDA, 4 additional matrices ( $\mathcal{L}$ ,  $\mathcal{R}$ ,  $\sigma_{\mathcal{L}\mathcal{R}}$  and  $\sigma_{\mathcal{R}\mathcal{L}}$ ) are stored, leading to

$$m_{\text{Dual-RDA}} \sim 12 \left( \frac{\dim \mathcal{H}}{K} \right)^2. \quad (26)$$

The data in fig. 5 (red) confirm these dependencies. For all CNTs with similar length and thus, similar number of slices  $K$ , the same linear dependence is achieved in the log-log-scale (indicated by one line), but reduced by a constant factor. The insets of fig. 5 show the same data, but with an abscissa, which is scaled with  $1/K$  ( $K = 1$  for the RDA). Here, all data points fall on one curve corresponding to (25) and (26) for the case  $K \ll a$ . The difference between the RDA and the Dual-RDA concerning calculation time in the inset of fig. 5(a) is exactly the factor of 2 caused by the 2 separate RDA calculations.

For the Multiple-RDA, where the bulk Green's function for the electrode density of states is additionally calculated, the comparison can be done a similar way. The calculation times compared to the ones of the conventional RDA are shown in fig. 6. For the conventional RDA nothing changes, because the calculation of the total bulk Green's function



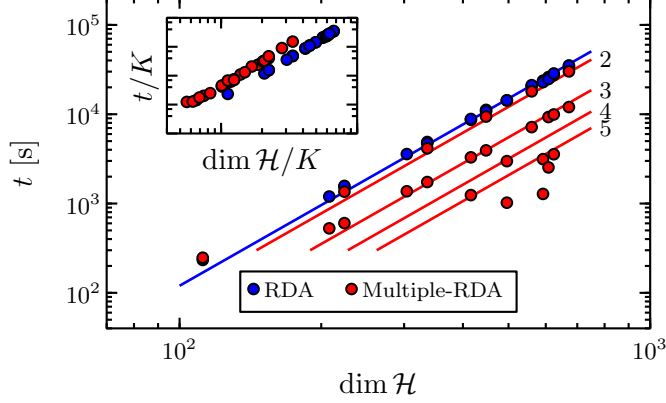


**Fig. 6:** (Color online.) Same as fig. 5(a) but for the Multiple-RDA, where the bulk Green's function additionally have to be computed.

is necessary for the calculation of the surface Green's functions. This leads to the same complexity measures (23) and (24). For the Multiple-RDA compared to the Dual-RDA this is not the case, because here the calculation of the total bulk Green's function can be partly omitted when only obtaining the surface Green's functions. Here, instead of calculating two surface blocks, all  $K$  bulk blocks have to be computed. In total, the Multiple-RDA described in sec. 4.2 needs for each of these  $K$  block  $K - 1$  decimation steps (1 matrix inversions, 6 matrix multiplications, and 2 matrix additions each), followed by 2 RDA executions, and afterwards additional 4 matrix inversions, 4 matrix multiplications, and 2 matrix additions to obtain the necessary diagonal and first non-diagonal matrix blocks. In total this yields  $K(K + 3 + 2a)$  matrix inversions,  $K(6K - 2 + 12a)$  matrix multiplications, and  $K(2K + 8a)$  matrix additions. As the dimension of the matrices is a factor of  $K$  smaller, the complexity measures yields

$$t_{\text{Multiple-RDA}} \sim K(K + 3 + 2a) \left( \frac{\dim \mathcal{H}}{K} \right)^3 \stackrel{K \ll a}{\approx} 2aK \left( \frac{\dim \mathcal{H}}{K} \right)^3, \quad (27a)$$

$$\stackrel{K \gg a}{\approx} K^2 \left( \frac{\dim \mathcal{H}}{K} \right)^3. \quad (27b)$$

The data are shown in fig. 6 (red) and confirm these dependencies. In the same way as for the Dual-RDA, a linear dependence is valid in the log-log-scale for CNTs with the same number of slices  $K$  (indicated by one line). In the inset the abscissa and the ordinate are scaled with  $1/K$  ( $K = 1$  for the RDA) to verify (27) for the case  $K \ll a$ . As all points lie on the same curve, this dependence is valid. The additional factor  $K$  compared to the Dual-RDA describes the  $K$ -fold amount of information which must be computed for the bulk Green's function compared to the surface Green's functions. Thus, the calculation time reduction is lower compared to the Dual-RDA. There is a small improvement for the shortest CNT unit cells and a reduction up to a factor of 18 for the longest CNT unit cells studied here. The difference between the RDA and the Multiple-RDA is exactly the factor of 2 caused by the 2 RDA calculations which are done for each bulk matrix block.

## 6 Exemplary results

Finally, we present some exemplary results for CNTs to show, that it is possible to calculate transport properties of materials with huge unit cells very effective. We use a density-functional-based tight-binding (DFTB) model [5, 6] and the parameter set 3ob of Gaus et al. [21], which is suitable for carbon materials and includes the 2s and the three 2p Slater-Koster orbitals [22]. We consider two CNTs: (A) The (10,1)-CNT as one of the biggest ones shown before in fig. 4 contains 148 atoms within one unit cell. (B) The even bigger (10,9)-CNT contains 1084 atoms within one unit cell. Fig. 7 presents the transmission spectrum and the density of states of these two CNTs. First, the transmission spectra for the periodic CNTs are depicted, including the calculations for 60 000 energy points. Second, the transmission spectra of CNTs which include one monovacancy (one removed atom) are depicted. Third, the electrode density of states of the periodic CNTs and the device density of states of the CNTs which include one monovacancy are shown. For both CNTs the MV defect leads to a significant reduction of the transmission, especially at energies slightly below the Fermi energy. For the (10,1)-CNT two features can be seen: a broad dip at approximately 0.5 eV below  $E_F$  and a sharp dip at approximately 0.2 eV below  $E_F$ . Comparing this with the device density of states, it can be seen that the dips in the transmission coincide with similar broad/sharp peaks in the density of states. These peaks are defect states which cause an localization of the wave function at the defect and thus reduce the transmission significantly. The (10,9)-CNT with a monovacancy shows only a tiny broad peak in the density of states at approximately 0.4 eV below  $E_F$ , leading to no additional features in the transmission spectrum.

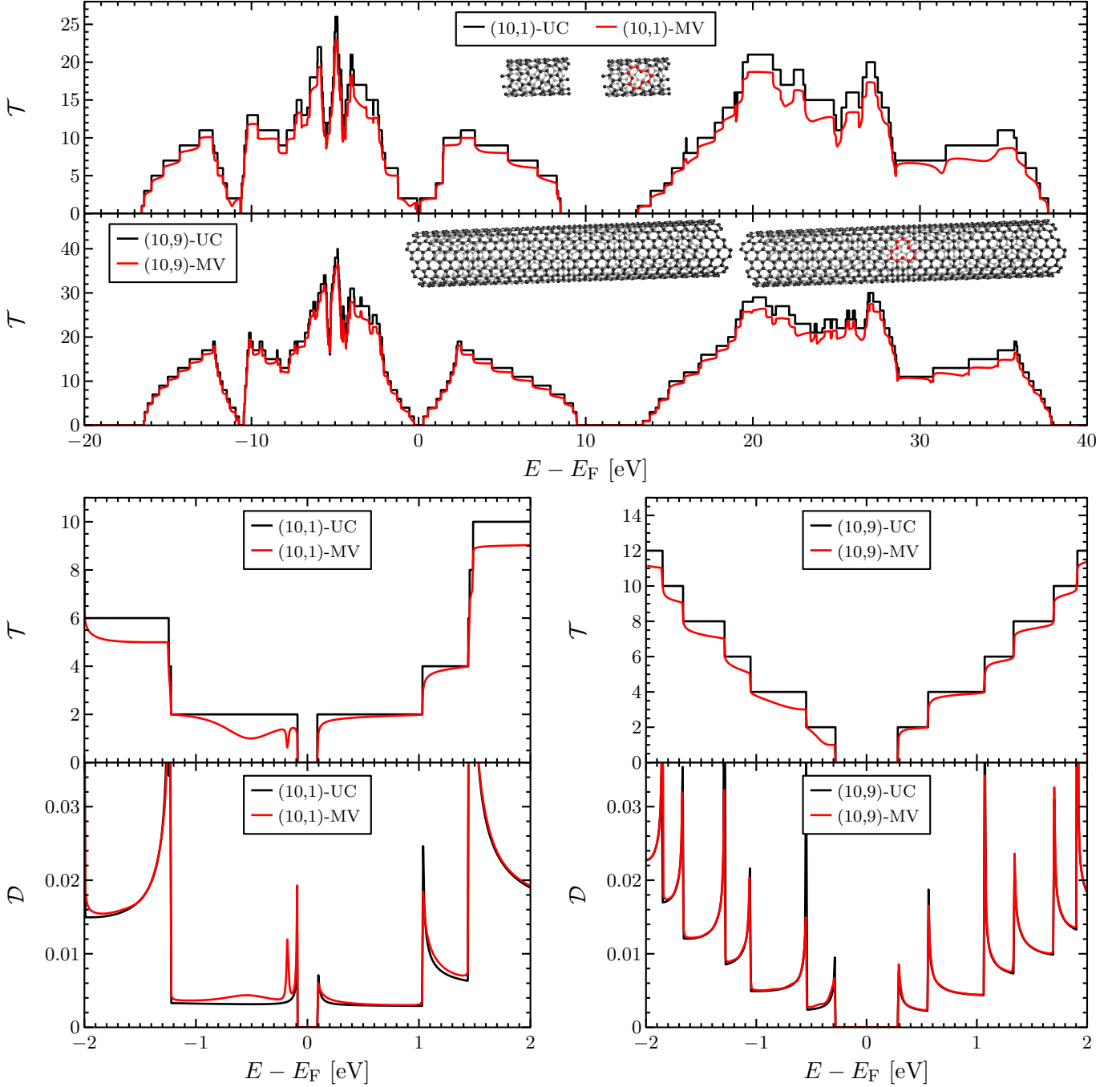


**Fig. 7:** (Color online.) (upper) Complete transmission spectrum  $\mathcal{T}$  of the (10,1) CNT and the (10,9)-CNT for the ideal, periodic case (black) and for a CNT with with one monovacancy (red). (center) Same results around the Fermi energy. (lower) Device density of states  $\mathcal{D}$  for the same structures.

Fig. 8 shows the dependence of the resistance and the conductance on the number of monovacancies at 300 K. The calculations have been performed using the recursive Green's function formalism (RGF) to treat huge central regions, which is also based on the decimation technique and leads to a linear scaling algorithm [16]. The data can be described by two distinct transport regimes. For less defects, the electrons are scattered at the defects, which leads to a reduction of the conductance for each additional defect. This is the diffusion regime, where the resistance increases linear with the number of defects [23]:

$$R \propto 1 + \frac{N}{N_{\text{mfp}}} \quad . \quad (28)$$

Here,  $N_{\text{mfp}}$  is the dimensionless elastic mean free path (normalized to the average defect distance). Above a certain number of defects, the increasingly strong scattering leads to destructive interference effects, which further reduce the conductance. This is the strong localization regime, where the conductance decreases exponentially with the number

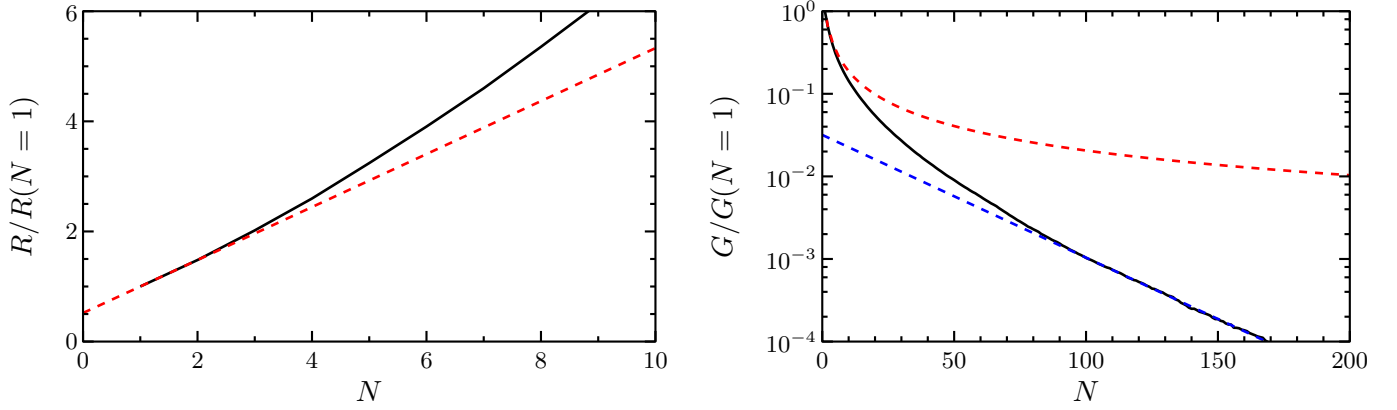


**Fig. 8:** (Color online.) (left) Resistance and (right) conductance of the (10,1)-CNT as a function of the number of MV defects (black straight lines) at 300 K. The data are normalized to the values for one MV defect. The straight lines are regressions concerning the diffusion regime (red) and the localization regime (blue).

of defects [24, 25]:

$$G \propto \exp\left(-\frac{N}{N^{\text{loc}}}\right) \quad . \quad (29)$$

Here,  $N^{\text{loc}}$  is the localization exponent (localization length normalized to the average defect distance). The regressions in fig. 8 show that both regimes fit very well. We get  $R = 0.52(1 + N/1.1)$  for the diffusion regime and  $G = 0.032\exp(-N/29)$  for the localization regime. Further results of electron transport through arbitrary chiral CNT can be found in our comprehensive study [13].

## 7 Summary and conclusions

In the first part, we developed an improved electrode algorithm for tight-binding-based quantum transport calculations of systems with very long unit cells in transport direction, like it is the case e.g. for chiral nanotubes and chiral nanoribbons. The Hamiltonian matrix of the electrodes are blockwise tridiagonal and always periodic, which is used in the common RDA to calculate the bulk Green's function and the left/right surface Green's functions. For the case of very long unit cells each matrix block is again blockwise tridiagonal, but not periodic. We showed how the common RDA can be improved for such cases by dividing the unit cells into  $K$  slices. We derived iterative equations for the surface Green's functions, which is needed to calculate the transmission function, as well as for the diagonal and the first non-diagonal blocks of the bulk Green's functions, which are needed to calculate the bulk density of states.

In the second part, we analyzed the complexity of the improved RDA. We showed that a factor  $K^3$  is gained for the transmission computation. If the bulk density of states is calculated, a factor  $K^2$  is gained. We applied the improved RDA to carbon nanotubes of different unit cell length. The extracted computation times verify the complexity scaling.

In the last part, we displayed some exemplary results for electron transport through (10,1) and (10,9) carbon nanotubes with monovacancy defects in the mesoscopic length scale. We showed that the conductance as a function of the number of defects can be described by diffusion regime for few defects. For a large amount of defects, the transport is driven into the strong localized regime. For these regimes, we extracted the elastic mean free path and the localization length.

This work contributes to the continuing development of numerical implementations in quantum transport theory. It may be useful for reducing the computation time of electron transport calculations of different systems with long unit cells like nanotubes, nanoribbons, and nanowires or also for defective supercell calculations.

## Acknowledgement

This work is funded by the European Union (ERDF) and the Free State of Saxony via the ESF project 100231947 (Young Investigators Group Computer Simulations for Materials Design - CoSiMa).



---

## References

- [1] S. Datta: Quantum Transport: Atom to Transistor 2005, Cambridge University Press, Cambridge.
- [2] M. Büttiker, Y. Imry, R. Landauer, and S. Pinhas: Generalized many-channel conductance formula with application to small rings, *Physical Review B* 31 (1985), 6207–6215.
- [3] K. Capelle: A Bird’s-Eye View of Density-Functional Theory, *Brazilian Journal of Physics* 36 (2006), 1318–1343.
- [4] M. Brandbyge, J.-L. Mozos, P. Ordejón, J. Taylor, and K. Stokbro: Density-functional method for nonequilibrium electron transport, *Physical Review B* 65 (2002), 165401.
- [5] D. Porezag, T. Frauenheim, T. Köhler, G. Seifert, and R. Kaschner: Construction of tight-binding-like potentials on the basis of density-functional theory: Application to carbon, *Physical Review B* 51 (1995), 12947–12957.
- [6] G. Seifert, D. Porezag, and T. Frauenheim: Calculations of molecules, clusters, and solids with a simplified LCAO-DFT-LDA scheme, *International Journal of Quantum Chemistry* 58 (1996), 185–192.
- [7] T. Markussen, R. Rurali, A.-P. Jauho, and M. Brandbyge: Scaling Theory Put into Practice: First-Principles Modeling of Transport in Doped Silicon Nanowires, *Physical Review Letters* 99 (2007), 076803.
- [8] B. Biel, F. J. García-Vidal, A. Rubio, and F. Flores: Ab initio study of transport properties in defected carbon nanotubes: an  $O(N)$  approach, *Journal of Physics: Condensed Matter* 20 (2008), 294214.
- [9] F. Flores, B. Biel, A. Rubio, F. J. García-Vidal, C. Gómez-Navarro, P. J. de Pablo, and J. Gómez-Herrero: Anderson localization regime in carbon nanotubes: size dependent properties, *Journal of Physics: Condensed Matter* 20 (2008), 304211.
- [10] F. Teichert, A. Zienert, J. Schuster, and M. Schreiber: Strong localization in defective carbon nanotubes: a recursive Green’s function study, *New Journal of Physics* 16 (2014), 123026.
- [11] G. Greene-Diniz, S. L. T. Jones, G. Fagas, M. Haverty, C. M. Lacambra, S. Shankar, and J. C. Greer: Divacancies in carbon nanotubes and their influence on electron scattering, *Journal of Physics: Condensed Matter* 26 (2014), 045303.
- [12] D. Teich, M. Claus, and G. Seifert: On the electronic and transport properties of semiconducting carbon nanotubes: the role of  $sp^3$ -defects, *Journal of Computational Electronics* 17 (2018), 521–530.
- [13] F. Teichert, A. Zienert, J. Schuster, and M. Schreiber: Electronic transport through defective semiconducting carbon nanotubes, In Preparation.
- [14] R. Haydock, V. Heine, and M. J. Kelly: Electronic structure based on the local atomic environment for tight-binding bands, *Journal of Physics C: Solid State Physics* 5 (1972), 2845–2858.
- [15] R. Haydock: The recursive solution of the Schrödinger equation, *Computer Physics Communications* 20 (1980), 11–16.
- [16] D. J. Thouless, and S. Kirkpatrick: Conductivity of the disordered linear chain, *Journal of Physics C: Solid State Physics* 14 (1981), 235–245.
- [17] A. MacKinnon: The calculation of transport properties and density of states of disordered solids, *Zeitschrift für Physik B Condensed Matter* 59 (1985), 385–390.
- [18] M. P. López Sancho, J. M. López Sancho, and J. Rubio: Highly convergent schemes for the calculation of bulk and surface Green functions, *Journal of Physics F: Metal Physics* 15 (1985), 851–858.
- [19] M. P. López Sancho, J. M. López Sancho, and J. Rubio: Quick iterative scheme for the calculation of transfer matrices: application to Mo (100), *Journal of Physics F: Metal Physics* 14 (1984), 1205–1215.
- [20] LAPACK - Linear Algebra PACKage, <http://www.netlib.org/lapack/>.
- [21] M. Gaus, A. Goez, and M. Elstner: Parametrization and Benchmark of DFTB3 for Organic Molecules, *Journal of Chemical Theory and Computation* 9 (2013), 338–354.
- [22] J. C. Slater, and G. F. Koster: Simplified LCAO Method for the Periodic Potential Problem, *Physical Review* 94 (1954), 1498–1524.
- [23] C. W. J. Beenakker: Random-matrix theory of quantum transport, *Reviews of Modern Physics* 69 (1997), 731–808.
- [24] A. MacKinnon, and B. Kramer: One-Parameter Scaling of Localization Length and Conductance in Disordered Systems, *Physical Review Letters* 47 (1981), 1546–1549.
- [25] E. Abrahams, P. W. Anderson, D. C. Licciardello, and T. V. Ramakrishnan: Scaling Theory of Localization: Absence of Quantum Diffusion in Two Dimensions, *Physical Review Letters* 42 (1979), 673–676.